Journal of Materials Chemistry C

Color tunable single-phase Eu^{2+} and Ce^{3+} co-activated Sr_2LiAlO_4 phosphors

Journal:	*Journal of Materials Chemistry C*
Manuscript ID	TC-ART-11-2018-005777.R2
Article Type:	Paper
Date Submitted by the Author:	17-May-2019
Complete List of Authors:	Ha, Jungmin; University of California San Diego, Materials Science and Engineering Program Kim, Yoon Hwa; Chonnam National University, School of Materials Science and Engineering Novitskaya, Ekaterina; University of California San Diego, Department of Mechanical and Aerospace Engineering Wang, Zhenbin; University of California, San Diego, Department of NanoEngineering Sanchez, Maritza; University of California San Diego, Materials Science and Engineering Program Graeve, Olivia; University of California San Diego, Department of Mechanical and Aerospace Engineering Ong, Shyue Ping; University of California, San Diego, Nanoengineering Im, Won Bin; Chonnam National University, School of Materials Science and Engineering McKittrick, Joanna ; University of California San Diego, Department of Mechanical and Aerospace Engineering; University of California San Diego, Materials Science and Engineering Program

Color tunable single-phase Eu^{2+} and Ce^{3+} co-activated Sr_2LiAlO_4 phosphors

Jungmin Ha[a], Yoon Hwa Kim[b], Ekaterina Novitskaya[c], Zhenbin Wang[d], Maritza Sanchez[a], Olivia A. Graeve[a,c], Shyue Ping Ong[d], Won Bin Im[b], Joanna McKittrick[a,c‡]

[a] Materials Science and Engineering Program,
[c] Department of Mechanical and Aerospace Engineering,
[d] Department of Nanoengineering,
University of California, San Diego, 9500 Gilman Dr., La Jolla, CA 92093, USA
[b] School of Materials Science and Engineering, Chonnam National University, 77 Yongbong-ro, Buk-gu, Gwangju 61186, Republic of Korea
‡ Corresponding author: Tel: 858-534-5425, Fax: 858-534-5698; E-mail: jmckittrick@ucsd.edu

ABSTRACT

High purity Eu^{2+} and Ce^{3+} singly and co-activated Sr_2LiAlO_4 phosphors were successfully synthesized through a facile combustion reaction. Fabrication of color tunable, single-phase phosphors was achieved by varying the Eu^{2+}/Ce^{3+} ratio that utilized the energy transfer between Ce^{3+} to Eu^{2+}. For the singly activated compositions, the highest quantum efficiencies were 25% and 40% for $Sr_{1.998}Eu_{0.002}LiAlO_4$ and $Sr_{1.998}Ce_{0.002}LiAlO_4$, respectively. The emission of $Sr_2LiAlO_4:Ce^{3+}$ and the excitation of $Sr_2LiAlO_4:Eu^{2+}$ overlap in the range of 400 nm - 500 nm, so that energy transfer from $Ce^{3+} \rightarrow Eu^{2+}$ takes place. The emission color of Eu^{2+} and Ce^{3+} co-activated Sr_2LiAlO_4 changes from blue, to cool-white, to green depending on the activator concentrations. The maximum quantum efficiency of Eu^{2+} and Ce^{3+} co-activated Sr_2LiAlO_4 was 55%, a 40% increase over the singly activated phosphors, which demonstrates that the quantum efficiency improves by co-activation.

KEYWORDS: Sr_2LiAlO_4, Eu^{2+}, Ce^{3+}, color tunable, solid state lighting

1. INTRODUCTION

Phosphor-converted white-light-emitting diodes (pc-WLEDs) are considered as the most promising next generation solid-state lighting technology due to their longer life time, superior efficiency, and low operating temperatures compared with traditional incandescent bulb and fluorescent lamp technologies [1-3]. Typical approaches to produce pc-WLEDs is a combination a blue-emitting (450 nm) InGaN LED with yellow-emitting phosphors ($Y_3Al_5O_{12}:Ce^{3+}$), but it suffers from a low color rendering index (CRI) value < 80 and high correlated color temperature CCT > 5000 K due to a lack of red emission [4-6]. To improve the CRI and CCT, an alternative approach is to utilize near-UV (380-420 nm) LEDs with a mixture of red, green, and blue (RGB) phosphors [7]. However, in the RGB phosphors converted system, the efficiency of blue emission is poor due to the strong re-absorption of blue light by the red and green phosphors. Single phase phosphors are considered as a possible solution to avoid this re-absorption issue [8-10]. In the LED device, heat generation occurs during LED lighting operation (~200ºC), leading to emission loss from the phosphors (thermal quenching) is also an important property to be considered [1, 11].

There are several methods to produce white light or color tunable light in single-phase phosphors with (1) single rare earth ions such as Eu^{3+}, Eu^{2+}, or Dy^{3+} as an activator in proper hosts [12, 13]; (2) the combination of multiple rare earth ions such as $Tm^{3+}/Tb^{3+}/Sm^{3+}$ and $Tm^{3+}/Tb^{3+}/Eu^{3+}$ emitting blue, green and yellow, or blue and yellow light [14]; (3) rare earth ion pair co-activators to use energy transfer mechanisms such as $Ce^{3+} \rightarrow Eu^{2+}$, $Ce^{3+}/Eu^{2+} \rightarrow Tb^{3+}$, $Eu^{2+} \rightarrow Mn^{2+}$, or $Ce^{3+} \rightarrow Mn^{2+}$ [15-24]; and (4) emission of white light by controlling the point defect concentration [25, 26].

In the rare-earth ion pair co-activators, luminescent properties of single phase phosphors with Ce^{3+} and Tb^{3+} have been reported [15, 17, 27-30], showing that the color could be adjusted

between blue- (Ce^{3+}) and green-, (Tb^{3+}) emissions, depending on the activator concentrations. For example, Jia et al. [15] reported a color tunable phosphor $NaBa_3La_3Si_6O_{12}:Ce^{3+},Tb^{3+}$. The emission of $NaBa_3La_3Si_6O_{12}:0.07Ce^{3+}$ was a broad band ranging from 340 nm to 500 nm in the blue emitting range for the excitation wavelength (λ_{ex}) of 331 nm. On the other hand, λ_{ex} of $NaBa_3La_3Si_6O_{12}:0.02Tb^{3+}$ were 268 nm and 378 nm. Energy transfer from $Ce^{3+} \rightarrow Tb^{3+}$ enhanced the green emission of Tb^{3+} due to the overlapping emission band of Ce^{3+} and excitation band of Tb^{3+} and color tunable emission from blue to green was achieved, depending on the Ce^{3+} and Tb^{3+} concentrations. Quantum efficiency (Φ) was not reported for this phosphor.

Single-phase phosphors activated by Ce^{3+} and Eu^{2+} have been studied for application in solid state lighting devices [18, 20-24]. For the blue emitting phosphor, co-activated $Ca_8La_2(PO_4)_6O_2:0.04Ce^{3+},0.02Eu^{2+}$ [20], Φ (43%) was enhanced compared to that of the single activator Eu^{2+} (13%). Furthermore, the color tunable (blue to yellow) phosphors $Li_2SrSiO_4:xEu^{2+}:0.01Ce^{3+}$ ($0.0025 \leq x \leq 0.01$) were studied to examine the energy transfer from $Ce^{3+} \rightarrow Eu^{2+}$ [21]. The emission intensity of Eu^{2+} was enhanced with Ce^{3+} co-activator although the Φ was not reported. Ce^{3+} and Eu^{2+} co-activated Ca_2BO_3Cl phosphors exhibited a color change from blue to yellow with $0.06Ce^{3+}$ and $0.015Eu^{2+}$ having CIE coordinates (0.326, 0.334) that are close to the white point (0.33, 0.33) [22]; however the Φ value was not reported. An emission wavelength shift from 461 to 494 nm was found for $Sr_{0.96-y}SiAl_2O_3N_2:0.04Ce^{3+},yEu^{2+}$ ($0 \leq y \leq 0.06$), because the emission from Eu^{2+} increased and the emission from Ce^{3+} decreased with an increase in y. The substitution of Ba in $Sr_{0.96-x}Ba_xSiAl_2O_3N_2:0.04Ce^{3+}:0.04Eu^{2+}$ ($0 \leq x \leq 0.92$) showed an emission shift from 491 nm to 505 nm, but Φ values were not reported. The series xEu^{2+} and yCe^{3+} in Li_2SrSiO_4 were prepared for white emission by a combinatorial approach [24]. A bright yellow luminescence was shown with $x = 0.005$ - 0.060 and $y = 0$. The yellow emission

decreased with an increase in the concentration of Ce^{3+}, emitting bright blue light with $x = 0$ and $y = 0.005$ - 0.050. The CIE color coordinates, Φ and thermal quenching at 150˚C were (0.359, 0.341), 27%, and 69%, respectively [1, 11]. These previous studies using Eu^{2+} and Ce^{3+} as co-activators in a single-phase phosphor demonstrated that color tunable ability can be achieved and Φ can be enhanced.

This is the first report on the preparation and analysis of co-activated $Sr_{2-x-y}Eu_xCe_yLiAlO_4$. Building on our recently reported phosphors [31], $Sr_{2-x}Eu_xLiAlO_4$ (green-emitting) and $Sr_{2-y}Ce_yLiAlO_4$ (blue-emitting) were used to explore the possibility of fabricating color-tunable, single phase compositions. The purity of Sr_2LiAlO_4 synthesized by combustion reaction was reported previously [31], however, the present work provides new findings on the effect of (1) post-annealing temperature on the amount of impurity phases and (2) the addition of excess Li ions to compensate for Li loss during processing. The optimum concentrations of Ce^{3+} or Eu^{2+} were determined and the emission color changes were examined as a function of the concentration of Ce^{3+} and Eu^{2}. The improved Φs are investigated in Eu^{2+} and Ce^{3+} co-activated combustion reaction powders.

2. EXPERIMENTAL PROCEDURE

2.1. Synthesis of Sr_2LiAlO_4 and $Sr_2LiAlO_4:Eu^{2+}/Ce^{3+}$

All chemicals were used without further purification. Synthesis of host Sr_2LiAlO_4, $Sr_{2-x}Eu_xLiAlO_4$ ($0.001 \leq x \leq 0.040$), $Sr_{2-y}Ce_yLiAlO_4$ ($0.001 \leq x \leq 0.040$), and $Sr_{2-x-y}Eu_xCe_yLiAlO_4$ ($0.0005 \leq x, y \leq 0.05$) were performed through the combustion reaction using $Sr_2(NO_3)_2$ (99.99%, Sigma Aldrich), $LiNO_3$ (ReagentPlus, Sigma Aldrich), $Al(NO_3)_3•9H_2O$ (ACS reagent, J. T. Baker), $Eu(NO_3)_3$ from Eu_2O_3 (99.99%, Alfa Aesar) with nitric acid (69.3%, Fisher Scientific),

and $Ce(NO_3)_3$ (99.99%, Alfa Aesar) as precursors, assisted by the exothermic reaction between urea (Certified ACS, Fisher Scientific) and ammonium nitrate (Certified ACS, Fisher Scientific) at 600°C.

For Solution 1, $Sr(NO_3)$, $LiNO_3$, and $Al(NO_3)_3$ in the molar ratio of 2:1:1 was added to 50 mL of deionized water in a 100 mL beaker with a magnetic stirrer. Solution 2 consisted of the desired amount of Eu_2O_3, which had been dissolved in 4 mL of nitric acid in a beaker to prepare $Eu(NO_3)_3$. For $Sr_{2-x}Eu_xLiAlO_4$, the desired amount of Solution 2 was introduced into Solution 1. For undoped Sr_2LiAlO_4, Solution 2 was not needed. For $Sr_{2-x}Ce_xLiAlO_4$, Solution 1 was used and the desired amount of $Ce(NO_3)_3$ was added. For $Sr_{2-x-y}Eu_xCe_yLiAlO_4$, Solution 2 and $Ce(NO_3)$ were introduced in Solution 1. Urea (1 g, CH_4N_2O) and ammonium hydroxide (1.3 g), with the molar ratio of urea/ammonium hydroxide = 1:1, were added into the solutions. After achieving transparency, it was poured into a large Pyrex beaker and placed into a muffle furnace at 600°C.

The solution boiled and after ~ 5 min. burst into flame due to the exothermic reaction of urea and the nitrates, producing a white-colored powder. The reaction during combustion is:

$$2Sr(NO_3)_2\,(s) + LiNO_3\,(s) + Al(NO_3)_3\,(s) + CH_4N_2O\,(s) + 3(NH_4)(NO_3)\,(s) \rightarrow Sr_2LiAlO_4\,(s) + 8N_2\,(g) + 10O_2\,(g) + 8H_2O\,(g) + CO_2\,(g)$$

Post-annealing was performed between 700 ºC and 850 ºC for 1-5 h in a $5\%H_2$ / $95\%N_2$ atmosphere to transform Eu^{3+} to Eu^{2+}. In some experiments, excess Li precursor was added in amounts up to 30 mol.% to compensate for Li sublimation during synthesis [32].

For comparison, powders were also synthesized by a solid-state reaction using powders of SrO (Kojundo, 99.9%), Li_2CO_3 (Kojundo, 99.9%), α-Al_2O_3 (Kojundo, 99.9%), and Eu_2O_3 (Kojundo, 99.9%) or CeO_2 (Kojundo, 99.99%). The starting materials were ground in an agate

mortar, placed in alumina crucibles and annealed at 900°C for 4 hours in a 25%H_2 / 75%N_2. Excess Li (10 wt.%) was added to compensate for Li evaporation [31].

2.2 Characterization

The powders were analyzed by X-ray diffraction (XRD, Bruker D2 Phaser, Karlsruhe, Germany) using CuKα radiation and a step size of 0.014° over a 2θ range of 20-80°. Structural information of the synthesized samples was derived by refinement using the TOPAS 4.2 software (Bruker) suite. The calculated XRD data were taken from Wang et al. [31] who first reported this structure. A field emission scanning electron microscope (FESEM, XL30, Philips, Amsterdam, Netherlands) at 10 keV was used to image the powders to determine their size and morphology. Samples were coated with iridium at 85 μA for 10 s before imaging. Quantum efficiency (Φ) measurements, photoluminescence (PL) emission, and excitation spectra were performed using a Hamamatsu C9920-02 (Hamamatsu City, Shizuoka, Japan) system. Absolute Φ measurements were performed using an integrating sphere system, with sodium salicylate (Φ = 44%) as a reference standard. Φ is the ratio of the number of photons absorbed by the sample with respect to the number of photons emitted from the sample (Φ = photons out / photons in). Color coordinates were obtained using ColorCalculator program (version 7.23, OSLAM SYLVANIA Inc., Beverly, MA, USA) by analyzing the emission spectra from the PL analysis. Thermal quenching analysis (25°C to 150°C) was performed using a custom designed device that consists of a heater, thermocouple, and the spectrophotometer.

3. RESULTS AND DISCUSSION

3.1 Synthesis of Sr_2LiAlO_4, and Eu^{2+}- or Ce^{3+}-activated Sr_2LiAlO_4

The optimal post-annealing condition was examined through XRD analysis (Figure 1a) resulting in the desired Sr_2LiAlO_4 phase with some impurities. The impurity peaks of $SrAl_4O_7$ and $Sr_2Al_6O_{11}$ are located at ~25º and ~27º, respectively. The post-annealing treatment at 700ºC for 1 hour produced 73 mol.% of Sr_2LiAlO_4 with 25 mol.% of $SrAl_4O_7$ and 2 mol.% of $Sr_2Al_6O_{11}$. The post-annealing at 800ºC for 1 hour reduced the amount of impurities (18 mol.% $SrAl_4O_7$, 3 mol.% $Sr_2Al_6O_{11}$), as illustrated in Figure 1a. After annealing at 850ºC for 5 h, the intensity of the (110) reflection at ~22º decreased, possibly arising from defects within the structure. The intensity in the XRD diffraction patterns is proportional to modulus squared of the structure factor, $I_{hkl} \propto |F_{hkl}|^2$ where the structure factor, F_{hkl}, is sum of the ionic location value that are proportional to ionic scattering factors, f_j [33]. When one or more ions are absent on the plane, the f_j value of the absent ions is equal to zero, therefore the value of F decreases along with the corresponding diffraction intensity. The intensity of the (110) reflection at ~22º decreased with the post-annealing of 850ºC for 5 h, indicating that the one or more ions are absent on the planes. The diffraction peak intensity decrease by vacancies present on the diffraction plane has been shown in earlier literature [34].

An impurity peak from $Sr_4Al_{14}O_{25}$ was also found at ~26º. The condition of 800ºC for 5 hours was selected as the optimal to obtain high crystallinity that typically occurs for high temperature annealing [35] and fewer impurities (7 wt.% $SrAl_4O_7$, 5 wt.% $Sr_2Al_6O_{11}$).

Due to the easy evaporation of Li ions during the synthesis or post-annealing process [32], the optimum concentration of excess Li ions to obtain high purity resultant material was analyzed by Reitveld refinement. The obtained R_{wp}, R_p, GOF values are presented in Table 1 for 1.10, 1.20, 1.25, and 1.30 mole fractions of Li, where R_{wp} is the weighted profiles residual factor, R_p is the profile residual factor and GOF is the goodness of fit [36]. R_p and R_{wp} show how well the

crystallographic model matches the experimental X-ray diffraction. Typically, the value of R_{wp} < 10% or GOF close to 1 is considered a close match. Figure 1b illustrates the XRD patterns for the selected concentrations of Li. The impurities, $SrAl_4O_7$ and $Sr_2Al_5O_{11}$, were reduced from 7 mol.% to 6 mol.%, and from 5 mol.% to 0 mol.%, respectively, when the Li concentration was 1.25 mole fraction. This demonstrates that Li evaporation occurred during the synthesis or annealing process. When the concentration increased to 1.30 mole fraction, more impurity peaks of $SrAl_4O_7$ appeared (Figure 1c), but $Sr_2Al_6O_{11}$ was not detected. In the calculated phase diagram SrO-Li_2O-Al_2O_3 [31] as shown in Figure 1d, $Sr_2Al_6O_{11}$ is located between $SrAl_2O_4$ and $SrAl_2O_7$, closer to the Sr_2LiAlO_4, and further away from Li_2O than $SrAl_4O_7$. Thus, the Li concentration affects the $Sr_2Al_6O_{11}$ stronger than $SrAl_4O_7$. Hence, the optimum processing conditions for Sr_2LiAlO_4 are a Li concentration of 1.25 mole fraction and an annealing treatment at 800ºC for 5 h, which results in a final purity of 94 mol.% with 6 mol.% of $SrAl_4O_7$ (Figure 1c). This is a higher purity compared to solid-state reaction powders (86 mol.%) [31] with 5 mol.% of $SrAl_4O_7$; 6 mol.% of $Sr_2Al_6O_{11}$, and 3 mol.% of SrO; thus the Φ of Eu^{2+} or Ce^{3+} activated Sr_2LiAlO_4 from combustion is expected to be higher than that from solid-state reaction. The XRD patterns of the Eu^{2+}- and Ce^{3+}- activated Sr_2LiAlO_4 are shown in Figure 1e. They are also well matched with the simulated Sr_2LiAlO_4 patterns previously reported [31].

Table 2 lists the calculated and experimental structure parameters of Sr_2LiAlO_4. The experimental *x*, *y*, *z* coordinates were found to be similar to the calculated *x*, *y*, *z* coordinates. The experimental and calculated unit cell parameters are provided in Table 3, showing a good match. The obtained residual values were R_{wp} = 12.14%, R_p = 8.81%, and GOF = 1.83, therefore, the experimental values are in good agreement with the calculated values (Table 2 and 3).

3.2 Photoluminescence spectra and quantum efficiency of Eu^{2+} or Ce^{3+} activated Sr_2LiAlO_4

The PL excitation (PLE) and PL emission spectra were measured for the Eu^{2+} or Ce^{3+} activated Sr_2LiAlO_4 (Figure 2). The PLE spectrum of $Sr_2LiAlO_4:Eu^{2+}$ was monitored at 515 nm and it showed two broad peaks centered at 390 nm and 315 nm. The PL emission spectra for this material (λ_{ex} = 390 nm) showed two broad peaks at 515 nm as a maximum and 565 nm as a shoulder (see Figure 2a). The two broad peaks in the PLE and PL are attributed to the two Sr^{2+} sites where Eu^{2+} was substituted [31]. Similar effects of two Sr^{2+} sites on the PL spectra have also been reported [31, 37, 38].To determine the optimal x in $Sr_{2-x}Eu_xLiAlO_4$, the PL emission spectra were analyzed for concentrations of $0.001 < x < 0.04$, as shown in Figure 2c. The corresponding intensities were normalized for x = 0.002, which had the maximum emission intensity with Φ = 25%, which was the same for the powders synthesized by the solid-state reaction.

The PLE of $Sr_2LiAlO_4:Ce^{3+}$ was measured under monitoring at 430 nm and it showed two peaks centered at 290 nm and 380 nm (dashed line in Figure 2b). The PL emission spectra (λ_{ex} = 380 nm) showed two broad peaks at 430 nm as a maximum and 470 as a shoulder (solid line in Figure 2b). These two broad peaks in the PLE and PL emission spectra are also from the two sites of Sr^{2+} where Ce^{3+} was substituted [31]. Several Ce^{3+} concentrations, $0.001 < y < 0.04$, were examined to obtain the optimum concentration, as shown in Figure 2c. The emission intensities were normalized for y = 0.002, which had the maximum emission intensity with Φ = 40%, which is higher than the powders synthesized by the solid-state reaction (32%) [31]. When there are impurities phases in Sr_2LiAlO_4, the activators are located in both impurities phases as well as in Sr_2LiAlO_4. The impurity content in the solid-state reacted powders ($SrAl_4O_7$, 5 mol.%; $Sr_2Al_6O_{11}$, 6 mol.%; SrO, 3 mol.%) is greater than in the combustion reactied powders ($SrAl_4O_7$, 6 mol.%). Therefore, the higher Φ of the combustion reacted powders (40%) than the solid-state reacted powders (32%) may be due to the reduced impurity content.

The Φ of $Sr_{1.998}Ce_{0.002}LiAlO_4$ was higher than the Φ of $Sr_{1.998}Eu_{0.002}LiAlO_4$ although the host lattice is the same. There are several examples that different activators (Eu^{2+} and Ce^{3+}) were in the same host lattice, but the Φs (or emission intensity) were also not similar between them. The Φs of Ba_2SiO_4:Eu^{2+} and Ba_2SiO_4:Ce^{3+} were 94% [39] and 69% [40], respectively. For $Ba_9Lu_2Si_6O_{24}$, the Φ for Eu^{2+} activation was 45% [41] and the Φ for Ce^{3+} activation was 82% [42]. Another example is $Ca_8La_2(PO_4)_6O_2$ where the Φs of the Eu^{2+} and Ce^{3+} activators were 14% and 67%, respectively [20]. Some phosphors showed higher Φ with Eu^{2+} than with Ce^{3+}, but other phosphors showed higher Φ with Ce^{3+} activator than with Eu^{2+} activator [20, 39-42]. This indicates that Φ depends on the host lattice, not activators and it needs to be further investigation.

Both $Sr_{2-x}Eu_xLiAlO_4$ and $Sr_{2-y}Ce_yLiAlO_4$ have a low optimum concentration x, y = 0.002 while the optimum activator concentration is typically > 0.01 [11, 39, 43]. Since concentration quenching is related to the distance between activators [44], the critical distance (R_c) between activators was calculated using [45]:

$$R_c = 2\left(\frac{3V}{4\pi x_c N}\right)^{1/3} \quad (1)$$

where x_c is the critical activator concentration when the emission intensity is the maximum value, V is the volume of the unit cell, and N is the total number cations in the unit cell in the host lattice. The obtained R_c, was 2.9 nm from V (0.209 nm^3), N (8), and X_c (0.002). This value of R_c is attributed to the small Stokes shift, arising from the stiffness of the host lattice from the AlO_4 tetrahedral network [46, 47]. For example, $Li_2Sr_{1-x}Eu_xSiO_4$ [48] also has a small optimal activator concentration (x = 0.005) with R_c = 3.4 nm, similar to the present work, which is also due to the small Stocks shift [48].

As shown in Figure 2, there are two emission peaks for both $Sr_{2-x}Eu_xLiAlO_4$ and $Sr_{2-y}Ce_yLiAlO_4$. According to Uitert [49], the emission wavelength of Eu^{2+} or Ce^{3+} ions strongly

depends on its local environment. The possible positions of the emission peaks can be estimated by the following equation [49-51]:

$$E(cm^{-1}) = Q\left[1 - \left(\frac{V}{4}\right)^{1/V} \times 10^{(-nrE_a)/8}\right] \quad (2)$$

where E is the position of the emission peaks from Eu^{2+} or Ce^{3+}, Q is the energy from the lower d-band edge of Eu^{2+} or Ce^{3+} ions (34,000 cm^{-1} for Eu^{2+} or 50,000 cm^{-1} for Ce^{3+} [49-51]), V is the valence of Eu^{2+} and Ce^{3+} (2 for Eu^{2+}, 3 for Ce^{3+}), n is the coordination number for Eu^{2+} or Ce^{3+} (n = 8 for both of Eu^{2+} and Ce^{3+}), E_a is the electron affinity of the anions (eV), and r is the radius (nm) of the cation replaced by Eu^{2+} or Ce^{3+}. The value of E_a for Sr_2LiAlO_4 was taken from that of aluminates [49], approximately, as 1.6 eV and r = 0.126 nm (8-coordinated Sr^{2+}). The calculated and experimental emission wavelengths for Eu^{2+} and Ce^{3+} are listed in Table 4. The calculated emission wavelengths of Eu^{2+} and Ce^{3+} were 529 and 466 nm, respectively, which were in a good agreement with the experimental values (515 nm and 565 nm for Eu^{2+}; 430 nm and 470 nm for Ce^{3+}). Although the host has two symmetrically distinct Sr sites [31], the sites have the same coordination number so that the E value has only one estimation for each activator. To compare these two experimental values with the one calculated value, the average experimental values were 540 nm for Eu^{2+} and 450 nm for Ce^{3+}, which are similar to the calculated values.

3.3 Thermal quenching properties and particle morphologies

The thermal quenching properties of $Sr_{1.998}Eu_{0.002}LiAlO_4$ and $Sr_{1.998}Ce_{0.002}LiAlO_4$ were measured and Figure 3a,b shows that as the temperature increases, the PL emission intensity for both materials decreases. For $Sr_{1.998}Eu_{0.002}LiAlO_4$, the emission intensity at 150ºC was 90% of the room temperature value, showing a very good thermal quenching property. Minimal thermal quenching means that in the host there are rigid bonding networks and high bond strength,

enabling minimization of the emission loss with increasing temperature [52]. The obtained good thermal quenching behavior implies that Sr_2LiAlO_4 has a rigid bonding network together with high bond strength. For $Sr_{1.998}Ce_{0.002}LiAlO_4$, a similar trend was observed, retaining 88% of emission intensity at 25ºC. This matches well with our previously reported value (91% of emission intensity at 25ºC for powders synthesized by the solid-state reaction) [31].

The SEM images of the $Sr_{1.998}Eu_{0.002}LiAlO_4$ and $Sr_{1.998}Ce_{0.002}LiAlO_4$ powders after annealing at 800ºC for 5 hours are shown in Figure 4a and Figure 4b, respectively. The particles were sub-micrometer sized, ~102 ±15 nm, non-aggregated and had a narrow size distribution. As shown, the morphology of powders was oval shaped with a smooth surface.

3.4 Luminescence properties of Eu^{2+} and Ce^{3+} co-activated Sr_2LiAlO_4

The excitation spectrum of $Sr_{2-x}Eu_xLiAlO_4$ partially overlaps with the emission spectrum of $Sr_{2-y}Ce_yLiAlO_4$ in the range of 400-500 nm (Figure 5a) and, therefore, the emission from $Sr_2LiAlO_4:Ce^{3+}$ can be partially re-absorbed by $Sr_2LiAlO_4:Eu^{2+}$, indicating that Ce^{3+} acts as a sensitizer for Eu^{2+} [53]. The Ce^{3+} is excited from $^7F_{5/2}$ to 5*d* energy level (λ_{ex} = 380 nm) and then returns to its ground state with visible light radiation. Photons in the Ce^{3+} 5*d* energy level transfer to the Eu^{2+} $4f^6 5d^1$ energy level, resulting in the Eu^{2+} $4f^6 5d \rightarrow 4f^7$, and then Eu^{2+} emits a green emission (~515 nm), as illustrated in Figure 5b. This process enables the emission intensity of Eu^{2+} to improve with the presence of Ce^{3+}. Since $Sr_{1.998-x}Eu_xCe_{0.0020}LiAlO_4$ and $Sr_{1.998-y}Eu_{0.0020}Ce_yLiAlO_4$ showed maximum emission intensities (Figure 2c), at concentrations of $0.0005 \leq x \leq 0.0050$ and $0.0005 \leq y \leq 0.0040$, they were selected to examine for improvement of the optical properties. For $Sr_{1.998-x}Eu_xCe_{0.0020}LiAlO_4$, the emission intensity of Ce^{3+} decreased when *x* increased, as shown in Figure 6a, which is attributed to the energy transfer from Ce^{3+} to Eu^{2+} [18]. Meanwhile, the emission intensity of Eu^{2+} increased up to $x = 0.0020$ owing to the Ce^{3+}

$\rightarrow Eu^{2+}$ energy transfer, remained constant and then decreased to $x = 0.0050$, which was attributed to concentration quenching. Figure 6b shows the change in the emission intensity of Eu^{2+} and Ce^{3+} depending on the Eu^{2+} concentration. For $Sr_{1.998-y}Eu_{0.0020}Ce_yLiAlO_4$, the emission intensity of Eu^{2+} increased from $y = 0.0005$ to 0.0010 and then decreased (Figure 6c), also attributed to the energy transfer from Ce^{3+} to Eu^{2+} [18]. Figure 6d shows the changes in the emission intensity for Eu^{2+} and Ce^{3+}. Although x is constant (0.002) and y increased, the emission intensity from Ce^{3+} leveled off for $y \geq 0.001$ after increasing from $y = 0.0005$ to 0.001. The emission intensity from Eu^{2+} increased until $y = 0.001$, and then decreased, attributed to the concentration quenching [11].

The energy transfer efficiency from Ce^{3+} to Eu^{2+} can be estimated by [54]:

$$\eta_T = 1 - {}^{I}/_{I_0} \quad (3)$$

where η_T is the energy transfer efficiency; I and I_0 are the emission intensities of the Ce^{3+} in the presence and absence of Eu^{2+}, respectively. Figure 6e shows the plot of η_T as a function of x ($0.0005 < x < 0.0050$) demonstrating that η_T increased with increase in x. For the concentrations of $x = y = 0.002$, $\eta_T =$ 55%, meaning that the 55% of the excited photons from the 5*d* level of Ce^{3+} transferred to the $4f^6 5d^1$ level of Eu^{2+} [8, 18, 55]. For x, $y = 0.005$, 0.002, $\eta_T = 92\%$, which demonstrates that the energy transfer from Ce^{3+} to Eu^{2+} depends on the concentration of Eu^{2+}, corroborating results of previous studies [18, 20-22].

For evaluation of the energy transfer mechanism from Ce^{3+} to Eu^{2+}, the following equation can be applied, based on Dexter energy transfer expressions of multipolar interaction and Reisfeld approximation [56, 57]:

$$log\left(\frac{I_0}{I}\right) \propto \frac{n}{3} log(C_{Eu^{2+} + Ce^{3+}}) \quad (4)$$

where *C* is the total concentration of Ce^{3+} and Eu^{2+}, and *n* is a function of electric multipolar character. Values of *n* = 6, 8, 10 correspond to dipole-dipole (*d*-*d*), dipole-quadrupole (*d*-*q*), and quadrupole-quadrupole (*q*-*q*) interactions, respectively. Figure 6f shows the plot of $log(I_0/I)$ as a function of $log(C_{Eu^{2+}+Ce^{3+}})$. The slope was found to be 2.21, resulting in $n \approx 6$, which corresponds to the *d*-*d* interaction. The energy transfer rate of *d*-*d* interaction is typically higher than that of *d*-*q* or *q*-*q* interactions [58]. In this case, the photons of the 5*d* level of Ce^{3+} are rapidly absorbed to the $4f^6 5d^1$ level of Eu^{2+}, leading to a shortened luminescent lifetime of Ce^{3+}. Previous studies have also shown that the energy transfer mechanism from Ce^{3+} to Eu^{2+} as the *d*-*d* interaction [58, 59].

Furthermore, concentration quenching can potentially be present in these co-activated phosphors due to the higher total activator concentration. The maximum Φ values (Table 5) for $Sr_{2-x-y}Eu_xCe_yLiAlO_4$ were 43% for *x*, *y* = 0.0010, 0 and 38% for *x*, *y* = 0, 0.0010. The highest PL intensities of $Sr_{1.997}Eu_{0.0010}Ce_{0.0020}LiAlO_4$ and $Sr_{1.997}Eu_{0.0020}Ce_{0.0010}LiAlO_4$ corresponded to *x* + *y* = 0.0030 are shown on Figure 6a and 6c. We selected a lower total activator concentration *x* + *y* = 0.0015 to determine if further improvement in Φ is possible. Figure 7a shows the PL emission spectra for *x*, *y* = 0.0005, 0.0010 and *x*, *y* = 0.0010, 0.0005, exhibiting a maximum emission intensity for *x*, *y* = 0.0005, 0.0010.

Table 5 lists Φ for the compositions studied. Figure 7b shows Φ as a function of *x* and *y*. For *x*, *y* = 0, 0.002, Φ = 40%, which is higher than that for solid-state reacted powders (32% for *x*, *y* = 0, 0.005 optimal concentration for solid-state reacted powders) [31]. With an increase in *x* and at constant *y* = 0.002, Φ increased from 40% for *x* = 0 to 43% for *x* = 0.0010. For $x \geq 0.0010$, the Φ value decreased due to the concentration quenching effect. For constant *x* = 0.002 and increasing *y*, Φ at *y* = 0 of the combustion reacted powders is 25%, same as the solid-state

reacted powders [31]. The Φ increased from 25% at $y = 0$ to 38% for $y = 0.0010$ and then decreased. The maximum Φ = 55% was found for $x, y = 0.0005, 0.0010$ and a slightly lower value of Φ = 51% for $x, y = 0.0010, 0.0005$; both showing at least a 40% increase over those for $x + y \geq 0.0020$. This is due to a lower total activator concentration that suppressed concentration quenching and improved Φ [44].

To analyze the effect of the energy transfer from Ce^{3+} to Eu^{2+}, the normalized ($x = 0.002$) emission intensity of Ce^{3+} for $Sr_{1.998-x}Eu_xCe_{0.002}LiAlO_4$ ($0.0005 \leq x \leq 00050$) is shown in Figure 8a. With an increase in x and at constant $y = 0.002$, the emission peak of Ce^{3+} was red-shifted from 427 nm to 433 nm as shown in Figure 8a,b. Piquette *et al*. [60] investigated on the radiative reabsorption and the red shift of the Ce^{3+} emission in $(Lu_{1-x}Ce_x)_3Al_5O_{12}$. Radiative reabsorption is when the emission photons are reabsorbed, which occurs when the emission and absorption bands overlap [60-62]. $(Lu_{1-x}Ce_x)_3Al_5O_{12}$ exhibits the partially overlap between the excitation and the emission of Ce^{3+}. The photons emitted in the lower wavenegth range were reabsorbed by Ce^{3+} in the higher wavelength range, causing emission wavelength red-shift. Although the radiative reabsorption was demonstrated in a single activator, this can be also applied to the co-activators in the case where the emission and the absorption of the co-activators overlap [63]. For example, in Eu^{2+}/Ce^{3+} co-activated $SrSc_2O_4$ it was reported that the red-shift of the Ce^{3+} emission was observed with an increase in Eu^{2+} [63]. For $Sr_{1.998-x}Eu_xCe_{0.002}LiAlO_4$, the excitation spectrum of Eu^{2+} and emission spectrum of Ce^{3+} partially overlap (Figure 5) resulting in radiative reabsorption of the Ce^{3+} emission by Eu^{2+} thereby red-shifting the Ce^{3+} emission.

3.5 Color coordinates and emission colors of Eu^{2+} and Ce^{3+} co-activated Sr_2LiAlO_4

Since $Sr_{2-y}Ce_yLiAlO_4$ and $Sr_{2-x}Eu_xLiAlO_4$ emit blue and green, respectively, the combination of Eu^{2+} and Ce^{3+} in Sr_2LiAlO_4 showed color tunable ability from blue to cool-white

and green emission. The color coordinates on the CIE diagram are listed in Table 5. The CIE chromaticity diagram and images of the powders under 365 nm UV light are shown in Figure 9. $Sr_{1.997}Eu_{0.002}Ce_{0.001}LiAlO_4$ (Φ = 38%) was in the cool-white region in the CIE diagram, having a CCT = 23450K, CRI = 60 and (0.2149, 0.2900) coordinates. The (*x*, *y*) coordinates changed linearly from (0.1472, 0.0972) for $Sr_{1.998}Ce_{0.002}LiAlO_4$ to (0.3324, 0.5732) for $Sr_{1.998}Eu_{0.002}LiAlO_4$, which is from blue to green emission. The phosphor powder photographs are also well matched with the color coordinate results, as presented in Figure 9. This indicates that the Eu^{2+} and Ce^{3+} co-activated Sr_2LiAlO_4 demonstrates good color tunable ability.

4. CONCLUSIONS

$Sr_{2-x}Eu_xLiAlO_4$ (green-emitting ~515 nm) and $Sr_{2-y}Ce_yLiAlO_4$ (blue-emitting ~430 nm) phosphors with 94% purity were prepared by the combustion synthesis method. The maximum quantum efficiencies were found for $Sr_{1.998}Eu_{0.002}LiAlO_4$ and $Sr_{1.998}Ce_{0.002}LiAlO_4$, (25% and 40%, respectively), which are higher then for solid state reacted powders. The emission intensities at 150°C of these compositions were 90% and 88% of the room temperature values, respectively, showing good thermal quenching resistance. For the first time, Eu^{2+} and Ce^{3+} co-activated Sr_2LiAlO_4 ($Sr_{2-x-y}Eu_xCe_yLiAlO_4$) were prepared to investigate the properties of color tunable single-phase phosphors. The emission color changed from blue, to cool-white, to green, depending on *x* and *y*. When *y* was constant and *x* increased, the emission intensity of Ce^{3+} decreased and that of Eu^{2+} increased, indicating that there was an energy transfer from Ce^{3+} to Eu^{2+}. With *x*, *y* = 0.005, 0.001, the maximum value of the quantum efficiency was 55%, an increase of 40% over those of the singlely activated powders. An increase in *x* at constant *y* = 0.002 exhibited a red shift of the emission spectra of Ce^{3+}, implying that radiative reabsorption occurred through the energy transfer from Ce^{3+} to Eu^{2+}. Eu^{2+} and Ce^{3+} co-activated Sr_2LiAlO_4

was found to be a promising color-tunable single-phase phosphor able to change color from blue, to cool-white and green for potential applications in phosphor converted white-emitting LEDs.

ACKNOWLEDGMENTS

This work is supported by the United States National Science Foundation, Ceramics Program Grant DMR-1411192. This work was performed in part at the San Diego Nanotechnology Infrastructure (SDNI) of UCSD, a member of the National Nanotechnology Coordinated Infrastructure, which is supported by the National Science Foundation (Grant ECCS-1542148).

REFERENCES

1. Y. H. Kim, P. Arunkumar, B. Y. Kim, S. Unithrattil, E. Kim, S.-H. Moon, J. Y. Hyun, K. H. Kim, D. Lee, J.-S. Lee and W. B. Im, *Nature Materials*, 2017, **16**, 543.
2. P. Pust, V. Weiler, C. Hecht, A. Tücks, A. S. Wochnik, A.-K. Henß, D. Wiechert, C. Scheu, P. J. Schmidt and W. Schnick, *Nature Materials*, 2014, **13**, 891.
3. S. Nakamura and G. Fasol, *The Blue Laser Diode*, Springer, Berlin, 1996.
4. V. V. Atuchin, N. F. Beisel, E. N. Galashov, E. M. Mandrik, M. S. Molokeev, A. P. Yelisseyev, A. A. Yusuf and Z. Xia, *ACS applied materials & interfaces*, 2015, **7**, 26235-26243.
5. H. Ji, L. Wang, M. S. Molokeev, N. Hirosaki, R. Xie, Z. Huang, Z. Xia, M. Otmar, L. Liu and V. V. Atuchin, *Journal of Materials Chemistry C*, 2016, **4**, 6855-6863.
6. E. Galashov, V. Atuchin, T. Gavrilova, I. Korolkov, Y. Mandrik, A. Yelisseyev and Z. Xia, *Journal of Materials Science*, 2017, **52**, 13033-13039.
7. S. Pimputkar, J. S. Speck, S. P. DenBaars and S. Nakamura, *Nature Photonics*, 2009, **3**, 180.
8. J. Hou, W. Jiang, Y. Fang and F. Huang, *Journal of Materials Chemistry C*, 2013, **1**, 5892-5898.
9. X. Piao, T. Horikawa, H. Hanzawa and K.-i. Machida, *Applied Physics Letters*, 2006, **88**, 161908.
10. M. Shang, C. Li and J. Lin, *Chemical Society Reviews*, 2014, **43**, 1372-1386.
11. J. Ha, Z. Wang, E. Novitskaya, G. A. Hirata, O. A. Graeve, S. P. Ong and J. McKittrick, *Journal of Luminescence*, 2016, **179**, 297-305.
12. C.-H. Huang, P.-J. Wu, J.-F. Lee and T.-M. Chen, *Journal of Materials Chemistry*, 2011, **21**, 10489-10495.
13. Z.-C. Wu, J. Liu, W.-G. Hou, J. Xu and M.-L. Gong, *Journal of Alloys and Compounds*, 2010, **498**, 139-142.
14. G. Li, Z. Hou, C. Peng, W. Wang, Z. Cheng, C. Li, H. Lian and J. Lin, *Advanced Functional Materials*, 2010, **20**, 3446-3456.
15. Z. Jia and M. Xia, *Scientific Reports*, 2016, **6**, 33283.
16. F. Ruan, D. Deng, M. Wu, C. Wu and S. Xu, *Journal of Luminescence*, 2018, **198**, 1-9.
17. D. Geng, M. Shang, D. Yang, Y. Zhang, Z. Cheng and J. Lin, *Dalton Transactions*, 2012, **41**, 14042-14045.
18. C. Xu, H. Guan, Y. Song, Z. An, X. Zhang, X. Zhou, Z. Shi, Y. Sheng and H. Zou, *Physical Chemistry Chemical Physics*, 2018.
19. Z. Wang, S. Lou, P. Li and Z. Lian, *Applied Optics*, 2017, **56**, 1167-1172.
20. M. Shang, G. Li, D. Geng, D. Yang, X. Kang, Y. Zhang, H. Lian and J. Lin, *The Journal of Physical Chemistry C*, 2012, **116**, 10222-10231.
21. H. He, R. Fu, Y. Cao, X. Song, Z. Pan, X. Zhao, Q. Xiao and R. Li, *Optical Materials*, 2010, **32**, 632-636.
22. C. Guo, L. Luan, F. G. Shi and X. Ding, *Journal of the Electrochemical Society*, 2009, **156**, J125-J128.
23. W.-Y. Huang, F. Yoshimura, K. Ueda, Y. Shimomura, H.-S. Sheu, T.-S. Chan, C.-Y. Chiang, W. Zhou and R.-S. Liu, *Chemistry of Materials*, 2014, **26**, 2075-2085.
24. L. Chen, A. Luo, Y. Zhang, F. Liu, Y. Jiang, Q. Xu, X. Chen, Q. Hu, S.-F. Chen and K.-J. Chen, *ACS Combinatorial Science*, 2012, **14**, 636-644.

25. A. M. Jakob and T. A. Schmedake, *Chemistry of Materials*, 2006, **18**, 3173-3175.
26. L. Ma, Z. Xia, V. Atuchin, M. Molokeev, S. Auluck, A. Reshak and Q. Liu, *Physical Chemistry Chemical Physics*, 2015, **17**, 31188-31194.
27. S. A. Khan, Z. Hao, H. Wei-Wei, L.-Y. Hao, X. Xu, N. Z. Khan and S. Agathopoulos, *Journal of Materials Science*, 2017, **52**, 10927-10937.
28. Z. Xia and R.-S. Liu, *The Journal of Physical Chemistry C*, 2012, **116**, 15604-15609.
29. N. Guo, Y. Song, H. You, G. Jia, M. Yang, K. Liu, Y. Zheng, Y. Huang and H. Zhang, *European Journal of Inorganic Chemistry*, 2010, **2010**, 4636-4642.
30. H. Y. Chung, C. H. Lu and C. H. Hsu, *Journal of the American Ceramic Society*, 2010, **93**, 1838-1841.
31. Z. Wang, J. Ha, Y. H. Kim, W. B. Im, J. McKittrick and S. P. Ong, *Joule*, 2018, **2**, 914-926.
32. V. Dotsenko, S. Levshov, I. Berezovskaya, G. Stryganyuk, A. Voloshinovskii and N. Efryushina, *Journal of Luminescence*, 2011, **131**, 310-315.
33. M. De Graef and M. E. McHenry, *Structure of Materials: An Introduction to Crystallography, Diffraction and Symmetry*, Cambridge University Press, 2012.
34. J. Makinson, J. Lee, S. Magner, R. De Angelis, W. Weins and A. Hieronymus, *Adv. X-Ray Anal*, 2000, **42**, 407-411.
35. J. Ha, E. Novitskaya, G. Hirata, C. Zhou, R. Ridley, O. Graeve and J. McKittrick, *Ceramics*, 2018, **1**, 5.
36. B. H. Toby, *Powder Diffraction*, 2006, **21**, 67-70.
37. H. Ji, Z. Huang, Z. Xia, M. S. Molokeev, V. V. Atuchin, M. Fang and S. Huang, *Inorganic chemistry*, 2014, **53**, 5129-5135.
38. H. Ji, Z. Huang, Z. Xia, Y. Xie, M. S. Molokeev and V. V. Atuchin, *Materials Research Bulletin*, 2016, **75**, 233-238.
39. J. K. Han, M. E. Hannah, A. Piquette, J. Micone, G. A. Hirata, J. B. Talbot, K. C. Mishra and J. McKittrick, *Journal of Luminescence*, 2013, **133**, 184-187.
40. J. Brgoch, S. P. DenBaars and R. Seshadri, *The Journal of Physical Chemistry C*, 2013, **117**, 17955-17959.
41. Y. Liu, C. Zhang, Z. Cheng, Z. Zhou, J. Jiang and H. Jiang, *Inorganic chemistry*, 2016, **55**, 8628-8635.
42. Y. Liu, J. Zhang, C. Zhang, J. Xu, G. Liu, J. Jiang and H. Jiang, *Advanced Optical Materials*, 2015, **3**, 1096-1101.
43. J. K. Han, M. E. Hannah, A. Piquette, G. A. Hirata, J. B. Talbot, K. C. Mishra and J. McKittrick, *Journal of Luminescence*, 2012, **132**, 106-109.
44. D. Dexter and J. H. Schulman, *The Journal of Chemical Physics*, 1954, **22**, 1063-1070.
45. G. Blasse, *Journal of Solid State Chemistry*, 1986, **62**, 207-211.
46. F. Lucas, S. Jaulmes, M. Quarton, T. Le Mercier, F. Guillen and C. Fouassier, *Journal of Solid State Chemistry*, 2000, **150**, 404-409.
47. A. Meijerink and G. Blasse, *Journal of Luminescence*, 1989, **43**, 283-289.
48. M. P. Saradhi and U. Varadaraju, *Chemistry of materials*, 2006, **18**, 5267-5272.
49. L. Van Uitert, *Journal of Luminescence*, 1984, **29**, 1-9.
50. J. Fan, J. Gou, Y. Chen, B. Yu and S. F. Liu, *Journal of Alloys and Compounds*, 2018, **731**, 796-804.
51. W. Geng, X. Zhou and Y. Wang, *RSC Advances*, 2016, **6**, 108964-108968.
52. G. Blasse, *The Journal of Chemical Physics*, 1969, **51**, 3529-3530.

53. C. R. Ronda, *Luminescence: From theory to applications*, 2008, 1-34.
54. J. Zhou and Z. Xia, *Journal of Materials Chemistry C*, 2015, **3**, 7552-7560.
55. K. Li, M. Shang, H. Lian and J. Lin, *Journal of Materials Chemistry C*, 2016, **4**, 5507-5530.
56. G. Blasse, *Physics Letters A*, 1968, **28**, 444-445.
57. H. Guan, Y. Song, K. Zheng, Y. Sheng and H. Zou, *Physical Chemistry Chemical Physics*, 2016, **18**, 13861-13873.
58. G. Caldino, *Journal of Physics-Condensed Matter*, 2003, **15**, 7127-7138.
59. L. Zhou, H. Liang, P. A. Tanner, S. Zhang, D. Hou, C. Liu, Y. Tao, Y. Huang and L. Li, *Journal of Materials Chemistry C*, 2013, **1**, 7155-7165.
60. A. P. Piquette, M. E. Hannah and K. C. Mishra, *ECS Transactions*, 2012, **41**, 1-9.
61. H. A. Höppe, H. Lutz, P. Morys, W. Schnick and A. Seilmeier, *Journal of Physics and Chemistry of Solids*, 2000, **61**, 2001-2006.
62. K. Sakuma, N. Hirosaki and R.-J. Xie, *Journal of Luminescence*, 2007, **126**, 843-852.
63. J. Zhao, X. Sun and Z. Wang, *Chemical Physics Letters*, 2018, **691**, 68-72.

TABLE AND FIGURE CAPTIONS

Tables

1. R_{wp}, R_p, and GOF values after Reitveld refinement for 1.00, 1.10, 1.20, 1.25, 1.30 mole fractions of Li ions in the starting material. R_{exp}: expected residual factor; R_{wp}: weighted profile residual factor; R_p: profile residual factor; GOF: goodness of fit.

2. Calculated [31] and experimental parameters of Sr_2LiAlO_4 prepared with 1.25 mole fraction of Li annealed at 800ºC for 5 h. The experimental values were obtained from X-ray diffraction Rietveld refinement of the combustion reaction samples. Values in parentheses are the estimated standard deviations of the last significant figure.

3. Experimental parameters after Rietveld refinement and calculated parameters [31] of Sr_2LiAlO_4 synthesized by the combustion reaction. Values in parentheses are the estimated standard deviations of the last significant figure.

4. Calculated and experimental emission wavelength of Eu^{2+} and Ce^{3+} in Sr_2LiAlO_4. *E* is the position of the emission peaks from Eu^{2+} or Ce^{3+}, *Q* is the energy from the lower *d*-band edge of Eu^{2+} or Ce^{3+} ions, *V* is the valence of Eu^{2+} and Ce^{3+}, *n* is the coordination number for Eu^{2+} or Ce^{3+}, E_a is the electron affinity of the atoms that form anions, and *r* is the radius of the cation replaced by Eu^{2+} or Ce^{3+}.

5. The color coordinates (*x*, *y*) and quantum efficiency (Φ) of $Sr_{2-x-y}Eu_xCe_yLiAlO_4$. (a)-(m) are the points shown on the CIE diagram in Figure 9.

Figures

1. X-ray diffraction patterns of Sr_2LiAlO_4 with **(a)** different post annealing conditions and **(b)** different concentration of Li ions. The simulation pattern was taken from [31]. **(c)** The ratio of Sr_2LiAlO_4 and impurities ($SrAl_4O_7$ and $Sr_2Al_6O_{11}$) with excess Li ions. **(d)** Calculated 0 K

SrO-Li_2O-Al_2O_3 phase diagram taken from [31]. **(e)** X-ray diffraction patterns of Sr_2LiAlO_4, $Sr_{2-x}Eu_xLiAlO_4$, and $Sr_{2-y}Ce_yLiAlO_4$.

2. Photoluminescence excitation (dashed line) and emission (solid line) of **(a)** $Sr_{2-x}Eu_xLiAlO_4$ and **(b)** $Sr_{2-y}Ce_yLiAlO_4$ **(c)** The normalized (to x or y = 0.002) emission intensities of Sr_2LiAlO_4:Eu^{2+} (green line) and $Sr_{2-y}Ce_yLiAlO_4$ (blue line) as a function of activator concentration.

3. Emission intensities as a function of temperature: **(a)** $Sr_{2-x}Eu_xLiAlO_4$ (λ_{ex} = 390 nm) and **(b)** $Sr_{2-y}Ce_yLiAlO_4$ (λ_{ex} = 380 nm). **(c)** Normalized (to room temperature) emission intensities of $Sr_{2-x}Eu_xLiAlO_4$ (green line) and $Sr_{2-y}Ce_yLiAlO_4$ (blue line).

4. Scanning electron microscope images of **(a)** $Sr_{2-x}Eu_xLiAlO_4$ and **(b)** $Sr_{2-y}Ce_yLiAlO_4$.

5. **(a)** Overlapped photoluminescence emission (solid line) and excitation (dashed line) of $Sr_{2-x}Eu_xLiAlO_4$ and $Sr_{2-y}Ce_yLiAlO_4$, respectively. **(b)** Scheme of energy transfer between Ce^{3+} and Eu^{2+} in Sr_2LiAlO_4, redrawn from [8].

6. **(a)** Photoluminescence emission spectra of $Sr_{1.998-x}Eu_xCe_{0.002}LiAlO_4$ and **(b)** plot of emission intensities of Eu^{2+} and Ce^{3+}. **(c)** Photoluminescence spectra of $Sr_{1.998-y}Eu_{0.002}Ce_yLiAlO_4$ and **(d)** plot of emission intensities of Eu^{2+} and Ce^{3+}**. (e)** Plot of the energy transfer efficiency as a function of Eu^{2+} concentration (x) in $Sr_{1.998-x}Eu_xCe_{0.002}LiAlO_4$. **(f)** Plot of $\log(I_0/I)$ as a function of $\log(C_{Eu^{2+}+Ce^{3+}})$.

7. **(a)** Photoluminescence spectra of $Sr_{1.9985-x-y}Eu_xCe_yLiAlO_4$ and **(b)** quantum efficiency as a function of activator concentration ($x + y \geq 0.0020$). Red circle and brown square are the efficiencies for a lower total activator concentration of $x + y = 0.0015$.

8. **(a)** Normalized (to x = 0.002) emission spectra from Ce^{3+} for $Sr_{1.998-x}Eu_xCe_{0.002}LiAlO_4$ ($0.0005 \leq x \leq 00050$). **(b)** Plot of the emission wavelength as a function x.

9. The CIE diagram showing coordinates of the phosphors and photographs of the powders $Sr_{2-x-y}Eu_xCe_yLiAlO_4$**.** The *x* and *y* values are shown in Table 5.

Table 1. R_{wp}, R_p, and GOF values after Reitveld refinement for 1.00, 1.10, 1.20, 1.25, 1.30 mole fractions of Li ions in the starting material. R_{exp}: expected residual factor; R_{wp}: weighted profile residual factor; R_p: profile residual factor; GOF: goodness of fit.

excess Li ions (mole fraction)	$\boldsymbol{R_{wp}}$	$\boldsymbol{R_p}$	**GOF**
1.00	13.22	9.17	2.55
1.10	13.79	9.76	2.45
1.20	11.75	8.02	2.12
1.25	12.14	8.81	1.83
1.30	17.81	13.07	2.93

Table 2. Calculated [31] and experimental parameters of Sr_2LiAlO_4 prepared with 1.25 mole fraction of Li annealed at 800ºC for 5 h. The experimental values were obtained from X-ray diffraction Rietveld refinement of the combustion reaction samples. Values in parentheses are the estimated standard deviations of the last significant figure.

site	**calculated**			**experimental**			**occupancy**	**Wyckoff position**
	x	*y*	*z*	*x*	*y*	*z*		
Sr1	0.22801	0.25000	0.43191	0.25226 (78)	0.25000	0.43390 (91)	1	2*e*
Sr2	0.27038	0.25000	0.94227	0.23642 (82)	0.25000	0.93358 (87)	1	2*e*
Li3	0.30224	0.75000	0.69253	0.2599 (50)	0.75000	0.6796 (60)	1	2*e*
Al4	0.27851	0.75000	0.19918	0.3016 (33)	0.75000	0.2027 (40)	1	2*e*
O5	0.47754	0.50758	0.25164	0.4998 (29)	0.5063 (33)	0.1906 (24)	1	4*f*
O6	0.09917	0.75000	0.37670	0.1082 (31)	0.75000	0.4291 (29)	1	2*e*
O7	0.11359	0.75000	0.92812	0.1579 (58)	0.75000	0.9050 (58)	1	2*e*

Table 3. Experimental parameters after Rietveld refinement and calculated parameters [31] of Sr_2LiAlO_4 synthesized by the combustion reaction. Values in parentheses are the estimated standard deviations of the last significant figure.

Experimental parameters		**calculated parameter**
crystal system	monoclinic	monoclinic
space group	$P2_1/m$	$P2_1/m$
a/nm	0.581565 (14)	0.58308
b/nm	0.563141 (16)	0.56386
c/nm	0.665946 (16)	0.66545
β/°	106.4558 (17)	106.70
volume/nm^3	0.2091658 (95)	0.20956
R_{exp} (%)	6.65	-
R_{wp} (%)	12.14	-
R_p (%)	8.81	-
GOF	1.83	-

Table 4. Calculated and experimental emission wavelength of Eu^{2+} and Ce^{3+} in Sr_2LiAlO_4. *E* is the position of the emission peaks from Eu^{2+} or Ce^{3+}, *Q* is the energy from the lower *d*-band edge of Eu^{2+} or Ce^{3+} ions, *V* is the valence of Eu^{2+} and Ce^{3+}, *n* is the coordination number for Eu^{2+} or Ce^{3+}, E_a is the electron affinity of the atoms that form anions, and *r* is the radius of the cation replaced by Eu^{2+} or Ce^{3+}.

activator	***Q* (cm^{-1})**	***V***	***n***	***r* (nm)**	**E_a (eV)**	***E* (nm)**	**E_{calc} (nm)**	**E_{exp} (nm)**
Eu^{2+}	34,000	2	8	0.126	1.6	1888.7	529	515, 565
Ce^{3+}	50,000	3	8	0.126	1.6	2144.2	466	430, 470

Table 5. The color coordinates (*x*, *y*) and quantum efficiency (Φ) of $Sr_{2-x-y}Eu_xCe_yLiAlO_4$. (a)-(m) are the points shown on the CIE diagram in Figure 9.

	$Sr_{2-x-y}Eu_xCe_yLiAlO_4$		CIE coordinates (*x*, *y*)	Φ (%)
	x	***y***		
(a)	0	0.0020	(0.1472, 0.0972)	40
(b)	0.0005	0.0020	(0.1636, 0.1849)	42
(c)	0.0010	0.0020	(0.1804, 0.1849)	43
(d)	0.0020	0.0040	(0.1907, 0.2221)	29
(e)	0.0020	0.0020	(0.2072, 0.2716)	32
(f)	0.0020	0.0010	(0.2149, 0.2900)	38
(g)	0.0020	0.0005	(0.2094, 0.2845)	36
(h)	0.0030	0.0020	(0.2302, 0.3382)	24
(i)	0.0040	0.0020	(0.2426, 0.4208)	18
(j)	0.0050	0.0020	(0.2503, 0.4344)	12
(k)	0.0020	0	(0.3324, 0.5732)	25
(l)	0.0005	0.0010	(0.1685, 0.1456)	55
(m)	0.0010	0.0005	(0.1846, 0.2100)	51

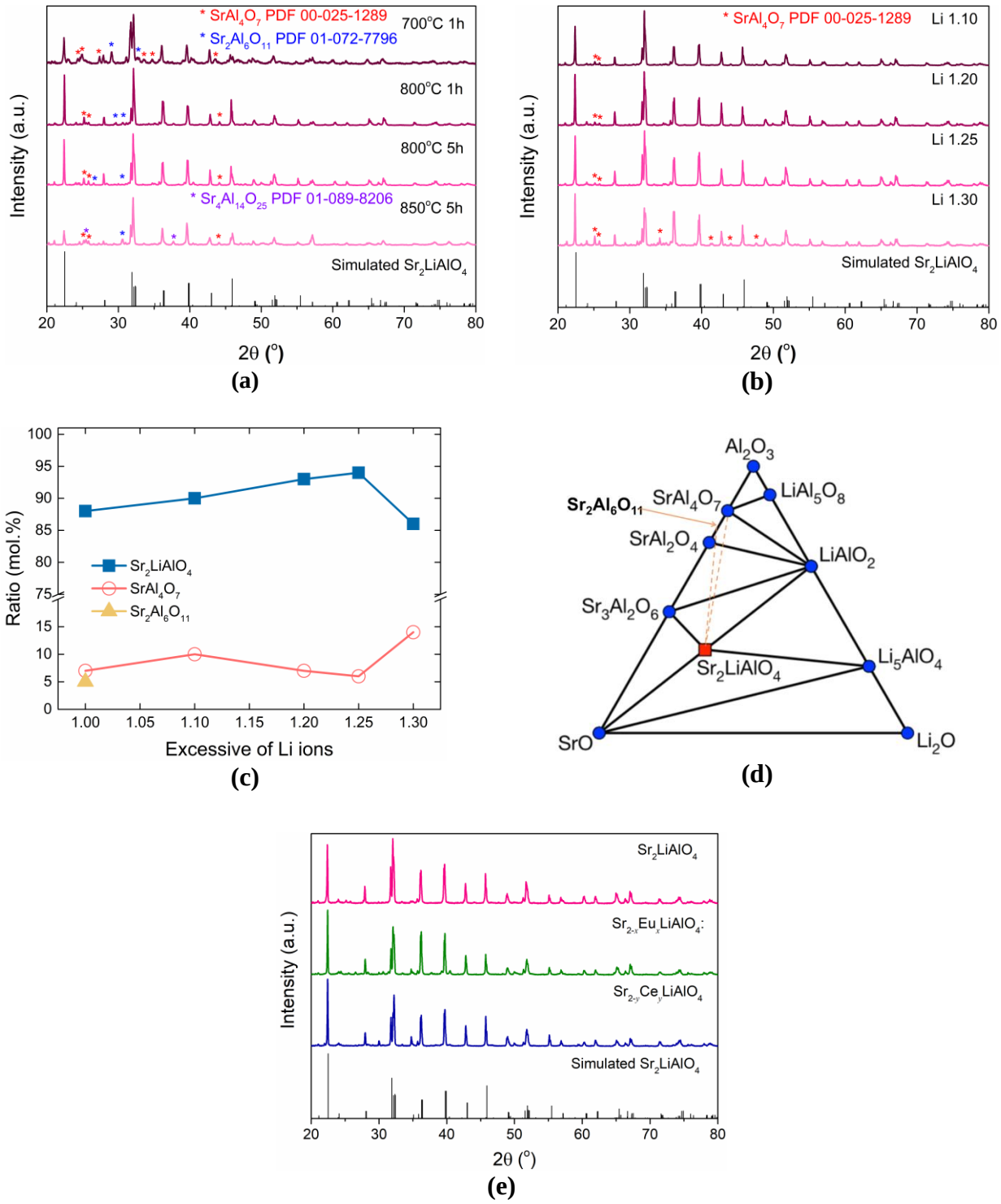

Figure 1. X-ray diffraction patterns of Sr_2LiAlO_4 with **(a)** different post annealing conditions and **(b)** different concentration of Li ions. The simulation pattern was taken from [31]. **(c)** The ratio of Sr_2LiAlO_4 and impurities ($SrAl_4O_7$ and $Sr_2Al_6O_{11}$) with excess Li ions. **(d)** Calculated 0 K SrO-Li_2O-Al_2O_3 phase diagram taken from [31]. **(e)** X-ray diffraction patterns of Sr_2LiAlO_4, $Sr_{2-x}Eu_xLiAlO_4$, and $Sr_{2-y}Ce_yLiAlO_4$.

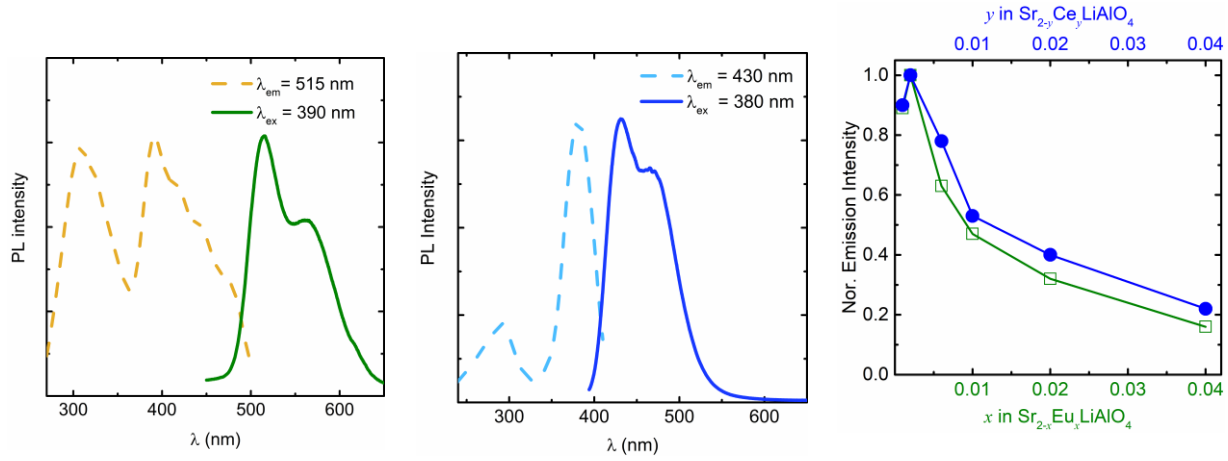

(a) **(b)** **(c)**

Figure 2. Photoluminescence excitation (dashed line) and emission (solid line) of **(a)** $Sr_{2-x}Eu_xLiAlO_4$ and **(b)** $Sr_{2-y}Ce_yLiAlO_4$. **(c)** The normalized (to x or y = 0.002) emission intensities of $Sr_{2-x}Eu_xLiAlO_4$ (green line) and $Sr_{2-y}Ce_yLiAlO_4$ (blue line) as a function of activator concentration.

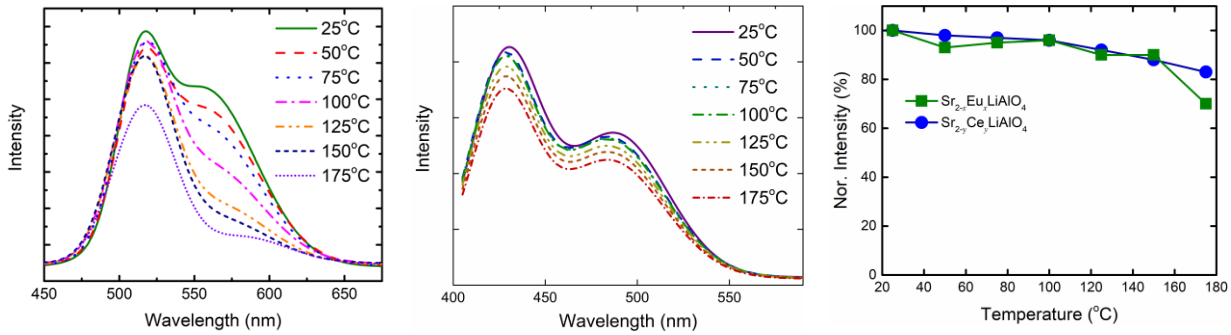

(a) **(b)** **(c)**

Figure 3. Emission intensities as a function of temperature: **(a)** $Sr_{2-x}Eu_xLiAlO_4$ (λ_{ex} = 390 nm) and **(b)** $Sr_{2-y}Ce_yLiAlO_4$ (λ_{ex} = 380 nm). **(c)** Normalized (to room temperature) emission intensities of $Sr_{2-x}Eu_xLiAlO_4$ (green line) and $Sr_{2-y}Ce_yLiAlO_4$ (blue line).

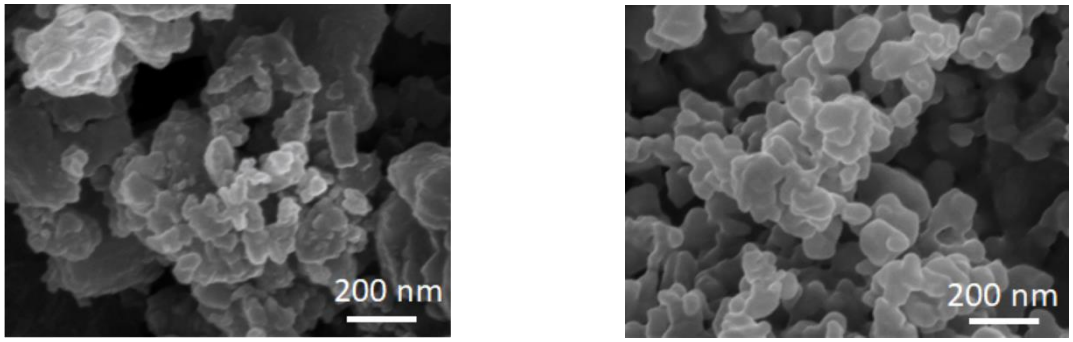

(a) **(b)**

Figure 4. Scanning electron microscope images of **(a)** $Sr_{2-x}Eu_xLiAlO_4$ and **(b)** $Sr_{2-y}Ce_yLiAlO_4$**.**

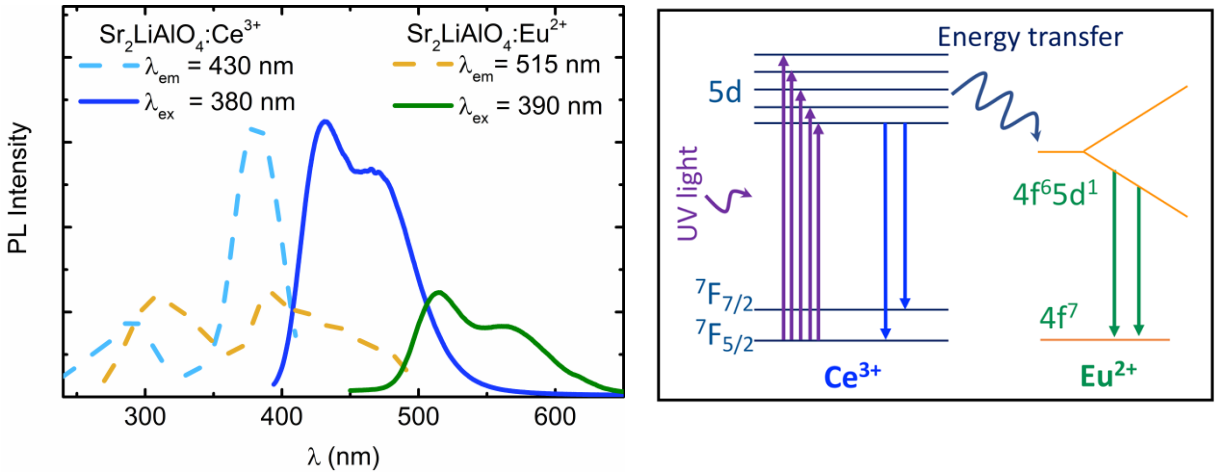

Figure 5. (a) Overlapped photoluminescence emission (solid line) and excitation (dashed line) of $Sr_{2-x}Eu_xLiAlO_4$ and $Sr_{2-y}Ce_yLiAlO_4$ respectively. **(b)** Scheme of energy transfer between Ce^{3+} and Eu^{2+} in Sr_2LiAlO_4, redrawn from [8].

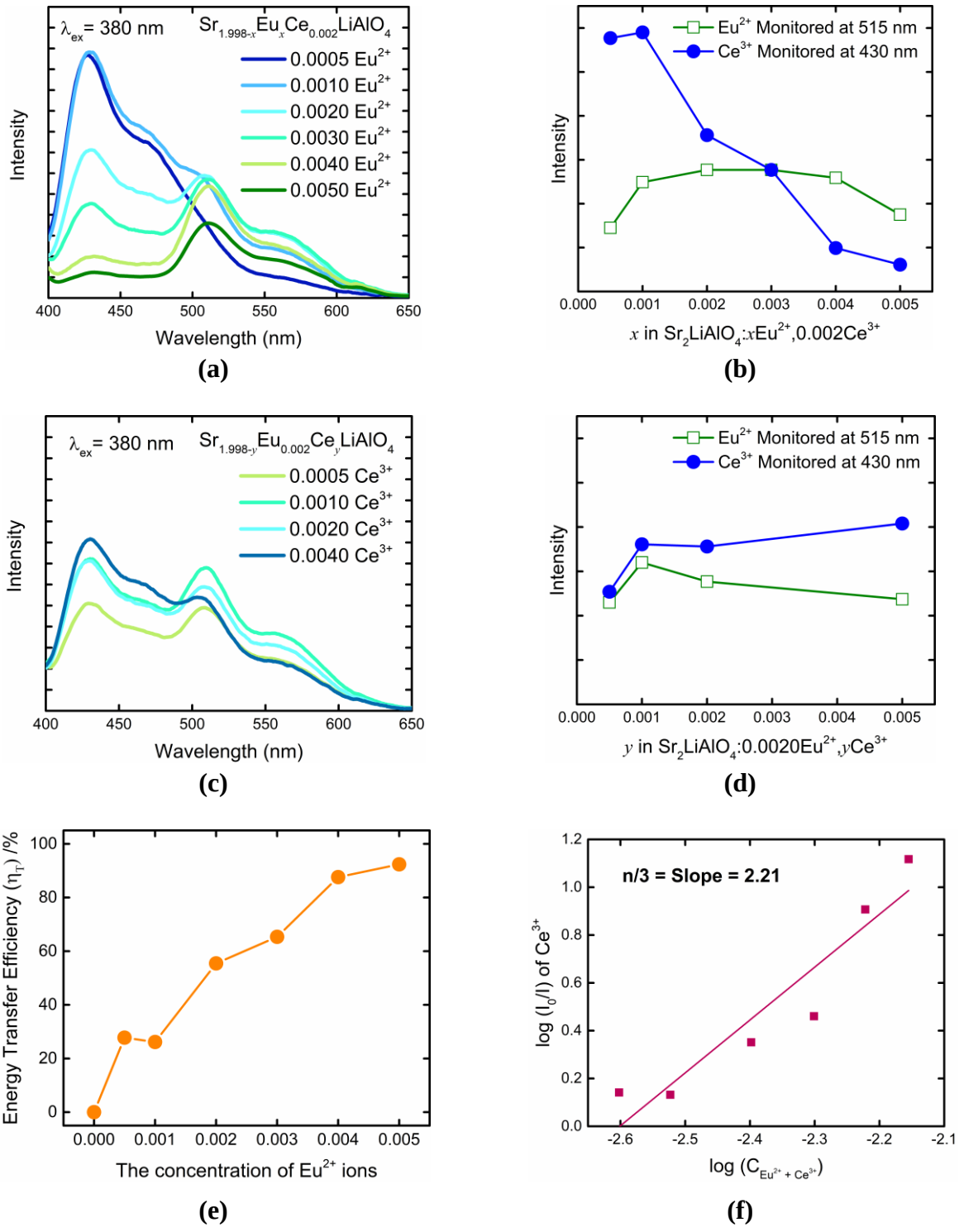

Figure 6. (a) Photoluminescence emission spectra of $Sr_{1.998-x}Eu_xCe_{0.002}LiAlO_4$ and **(b)** plot of emission intensities of Eu^{2+} and Ce^{3+}. **(c)** Photoluminescence spectra of $Sr_{1.998-y}Eu_{0.002}Ce_yLiAlO_4$ and **(d)** plot of emission intensities of Eu^{2+} and Ce^{3+}**. (e)** Plot of the energy transfer efficiency as a function of Eu^{2+} concentration (x) in $Sr_{1.998-x}Eu_xCe_{0.002}LiAlO_4$. **(f)** Plot of $\log(I_0/I)$ as a function of $\log(C_{Eu^{2+}+Ce^{3+}})$.

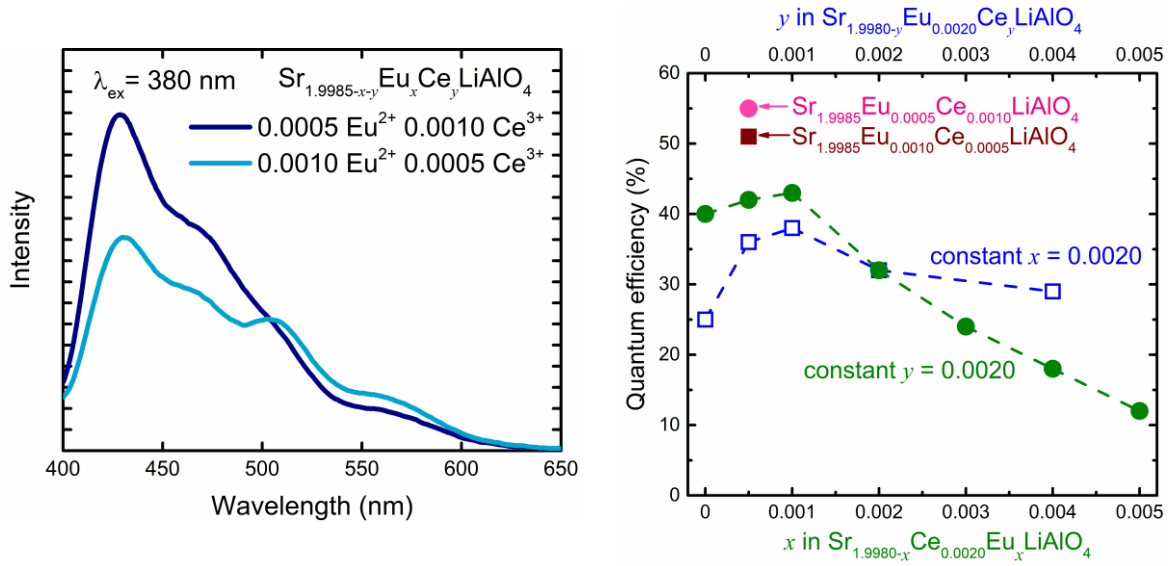

(a) **(b)**

Figure 7. (a) Photoluminescence spectra of $Sr_{1.9985-x-y}Eu_xCe_yLiAlO_4$ and **(b)** quantum efficiency as a function of activator concentration ($x + y \geq 0.0020$). Red circle and brown square are the efficiencies for a lower total activator concentration of $x + y = 0.0015$.

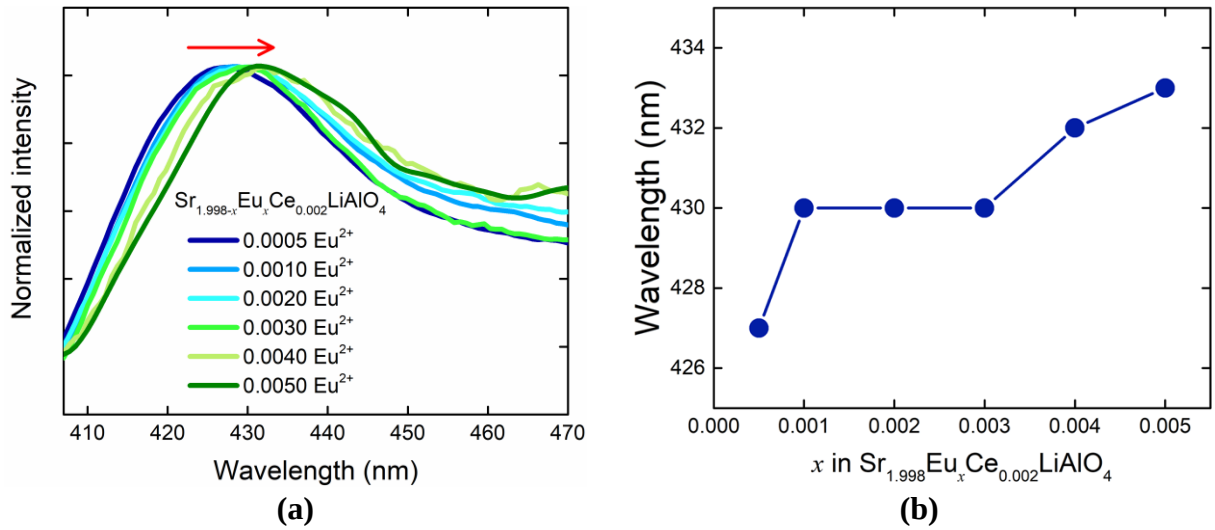

Figure 8. (a) Normalized (to $x = 0.002$) emission spectra from Ce^{3+} for $Sr_{1.998-x}Eu_xCe_{0.002}LiAlO_4$ ($0.0005 \leq x \leq 00050$). (b) Plot of the emission wavelength as a function x.

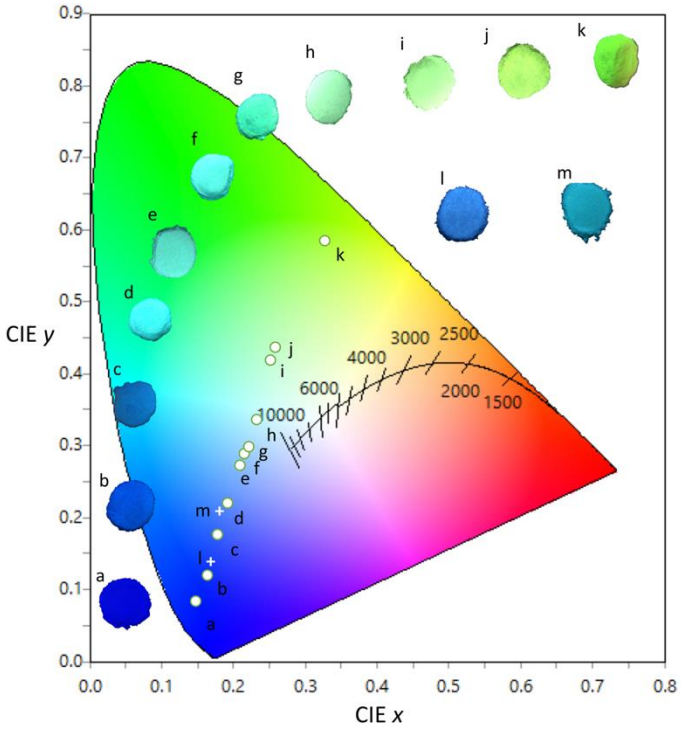

Figure 9. The CIE diagram showing coordinates of the phosphors and photographs of the powders $Sr_{2-x-y}Eu_xCe_yLiAlO_4$**.** The *x* and *y* values are shown in Table 5.

A table of contents entry

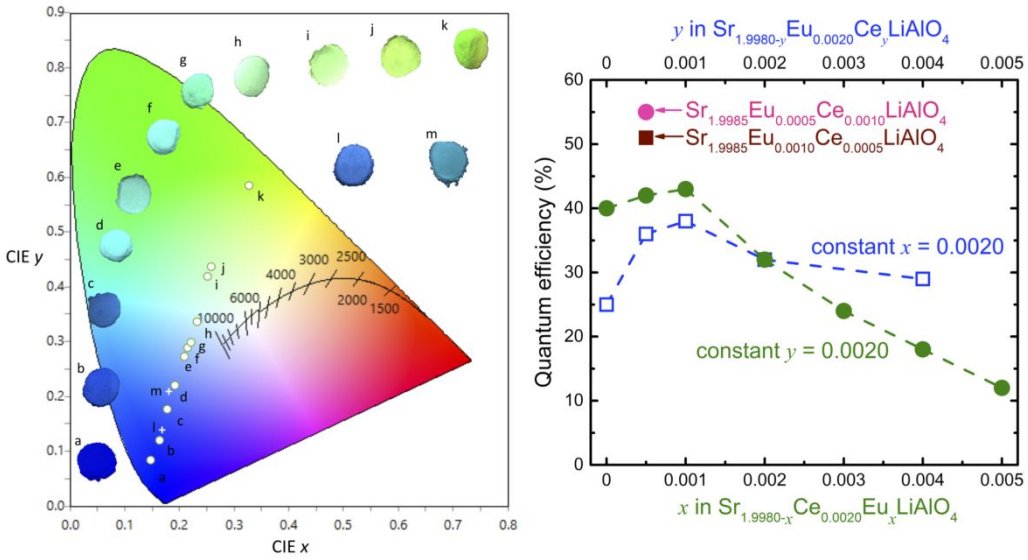

Color tunable single-phase phosphors (blue- to green-emitting) were fabricated with co-activators that also improved the quantum efficiency.